This is the author's accepted manuscript of a paper that was accepted for publication in the Journal of Composite Materials. A final version has been published as:

Flores-Johnson EA, Townsend J, Wang Z, Reiner J, Kruzic JJ. Numerical simulations of the splitting tensile behaviour of needle-punched carbon/carbon composites. *Journal of Composite Materials*. 2025;59(17):2057-2072. doi: https://doi.org/10.1177/00219983251318603

Numerical simulations of the splitting tensile behaviour of needle-punched carbon/carbon composites

Emmanuel A Flores-Johnson [a,b,*], Joshua Townsend [a,b], Zhiyang Wang [a,b], Johannes Reiner [c], Jamie J Kruzic [b]

[a] Australian Nuclear Science and Technology Organisation (ANSTO), Lucas Heights, NSW 2234, Australia

[b] School of Mechanical and Manufacturing Engineering, University of New South Wales (UNSW Sydney), Sydney, NSW 2052, Australia

[c] School of Engineering, Faculty of Science Engineering and Built Environment, Deakin University, Geelong, VIC 3220, Australia

*Corresponding author: floresje@ansto.gov.au

Abstract

Carbon/carbon (C/C) composites are materials developed for applications requiring excellent mechanical and thermal properties at elevated temperatures. Needle-punching has been used to improve the delamination resistance of C/C composites; however, its effect on tensile behaviour has yet to be fully understood. This work studies the splitting tensile behaviour of needle-punched C/C composites numerically using experimentally validated finite element (FE) simulations with a damage initiation criterion. The splitting tensile test, comprising the diametral loading of flattened Brazilian discs (FBDs), was employed for the simulations and validation. A mesoscale model of the composite FBD specimen was built, in which each composite layer was explicitly modelled, including cohesive interfacial behaviour. The composite needle fibre bundles were modelled using truss elements. The FE simulations showed the crucial role that needled fibre bundles play in the C/C composite tensile performance by carrying tensile stresses perpendicular to the loading direction and reducing the levels of localised deformation in the central region of the specimen at the early stages of loading. Furthermore, the damage initiation criterion showed that when the needle fibre bundles are included in the FE simulation, the extension of damaged areas is less than in the simulations without needled fibre bundles. In addition, the numerical results showed that increasing the number of needled fibre bundles reduced the extension of the damage in the matrix.

Keywords: Carbon/carbon composite; needle-punched composite; splitting tensile test; flattened Brazilian disc; finite element simulation; damage initiation criterion; cohesive interface

1. Introduction

Carbon/carbon (C/C) composites are composite materials comprising carbon fibres reinforcing a carbonaceous matrix, usually carbon or graphite. C/C composites were initially developed for aerospace applications due to their low density, high thermal conductivity, low coefficient of thermal expansion, and excellent mechanical properties at elevated temperatures.[1] Also, C/C composites can maintain high mechanical strength at temperatures up to 3000 °C in non-oxidising atmospheres.[2-6] C/C composite applications include rocket nozzles, re-entry vehicles' leading edges and nose tips, and aircraft brake discs.[1, 2, 7, 8] Other applications include, for instance, brake systems for racing cars,[9] manufacturing applications such as sintering trays[1] and hot pressing moulds,[10] and biomedical implants.[11] However, the use of C/C composites in general engineering industries, i.e., non-aerospace applications, is limited due to the high costs of manufacturing and machining this material,[12, 13] which has also limited the scientific research on C/C composites.

C/C composites have also been studied for their use in the nuclear energy generation industry. Popp et al.[14] investigated using C/C composites in hot gas ducts for nuclear reactors and showed that C/C composites were an excellent alternative to metals for this application. Venugopalan et al.[15] found that C/C composites coated with silicon carbide have an improved oxidation resistance, demonstrating that C/C composites are a potential candidate for structural materials for reactor applications. More recently, with the development of Generation IV nuclear reactors,[16] the need for materials with excellent mechanical properties at elevated temperatures has increased. Since then, C/C composites have been further developed and have been identified as candidate materials for their use in components of Generation IV nuclear reactors, such as control rods, hot duct assembly, or heat exchangers,[17] particularly for the very-high-temperature reactor (VHTR) and the molten salt reactor (MSR).[17-20] C/C composites are also being considered for structural components in fusion energy reactors.[21] However, to design safe components for nuclear applications made of C/C composites, it is crucial to understand the mechanical behaviour, damage resistance, and failure mechanisms under different loading conditions.[13, 22]

Traditional two-dimensional (2D) C/C composites, i.e., composite laminates, often exhibit limited interlaminar bonding strength,[23] making them prone to delamination. Improved delamination resistance can be achieved by producing three-dimensional (3D) composites using stitching or Z-pinning,[24] needle-punching,[25] and 3D woven or braided preforms.[24, 26, 27] The 3D needle-punching process is less complex and relatively cheaper than

other 3D preform manufacturing techniques.[25] In the needle-punching process, the composite preform containing layers of short-cut fibre web is punched with hook-fitted (barbed) needles, which push the web layer fibres into the cloth layers in the through-thickness direction, effectively attaching adjacent layers and creating a 3D structure.[25, 28-30] Zhang et al.[31] investigated the compressive behaviour of needle-punched C/C composites loaded in the longitudinal direction (load perpendicular to the through-thickness direction). They concluded that the primary failure-initiating mechanisms were fibre cloth layer delamination and debonding of interfaces. Tan et al.[11] investigated the tensile behaviour of needle-punched C/C composites and found that the specimens failed in a brittle fashion, exhibiting a complete transverse fracture. The tensile behaviour of C/C composites is usually analysed using rectangular specimens, which typically require a large amount of expensive C/C composite material. As an alternative test to use reduced sample size, the splitting tensile strength test, also known as the Brazilian disc test, can be employed, which is an indirect method to determine the tensile strength of brittle materials such as rocks,[32] granite,[33] ceramics[34] and graphite.[35, 36] It has also been used to test transversely isotropic materials,[37] fibre-reinforced polymer composites[38] and C/C composites.[39] For the Brazilian disc test, a thin circular disc is diametrically compressed to failure, inducing tensile stresses perpendicular to the compression loading direction in the central region of the specimen.[32] Flores-Johnson et al.[40] indirectly investigated the tensile behaviour of needle-punched C/C composites using the splitting tensile strength test on flattened Brazilian disc specimens. They found that the needle fibre bundles enabled different energy-absorbing failure mechanisms and globalised deformation.

The mechanical behaviour of needle-punched C/C composites using finite element (FE) simulations has also been investigated; however, the available work in the open literature is scarce. In addition, developing FE simulations for predicting the mechanical behaviour of C/C composites could reduce the costs of investigating this expensive material. Yu et al.[41] used a reconstructed FE model based on micro-CT images to model a representative volume element (RVE) using solid elements containing all the microscopic characteristics of the C/C composite, including the needled fibre bundles. Using this model, they predicted tensile stress-strain curves with good agreement with the experimental data. Xie et al.[42] used a multiscale model with solid elements to explicitly simulate the needled fibre bundles and the different layers of a C/C composite subjected to impact loading. They found that the FE model could predict the ballistic impact limit of different composite panel configurations.

Employing 3D solid elements to explicitly model the needled fibre bundles in a needle-punched C/C composite can lead to more accurate results; however, these models take more time to build and require extensive computational resources due to the large number of elements used to capture all the composite features. Another approach is using truss or beam elements to model bundles of fibres. For example, truss elements have been used to model polymer-matrix[43] and cement-based[44] fibre-reinforced composites and C/C composites.[45] Han et al.[45] investigated the tensile properties of needled C/C composites using solid elements for the different composite layers and beam elements to represent the needled fibre bundles. They found that using mixed solid and beam elements could predict the tensile response of C/C composites.

Based on the literature above, there is still a need for more available data on the tensile behaviour of needle-punched C/C composites. Moreover, a study showing the effects of the needle fibre bundles and their distribution on the splitting tensile behaviour of C/C composites has yet to be reported in the literature. Hence, this paper reports numerical results of the splitting tensile test of needle-punched C/C composites using flattened Brazilian discs (FBDs). Finite element (FE) simulations with experimental validation of FBDs were performed to investigate the effect of the needled fibre bundles on influencing the splitting tensile behaviour and damage of needle-punched C/C composites.

2. Numerical simulations

2.1. Problem description

The primary purpose of this study was to numerically investigate the effect of the needled fibre bundles on the splitting tensile behaviour of needle-punched composites. It is mentioned that the experimental results used to validate the numerical model have been presented elsewhere;[40] however, details of the 3D needle-punched C/C composite used in the validation and construction of the FE model composite numerically investigated here are provided as follows: The studied needle-punched C/C composite had the following layering sequence:[19, 40] 0° non-woven fibre cloth of T700 carbon fibres with a diameter of 7 μm (Toray Industries Inc., Japan),[46] short-cut fibre web of HTS40 carbon fibres with a diameter of 7 μm (Toho Tenax Co. Ltd., Japan)[47] and 90° non-woven cloth of T700 carbon fibres (Fig. 1a).[40] The overall fibre volume fraction of the C/C composite reported by the manufacturer is

30%.[19] As schematically shown in Fig. 1a, the needle fibre bundles were parallel to the Z-direction.

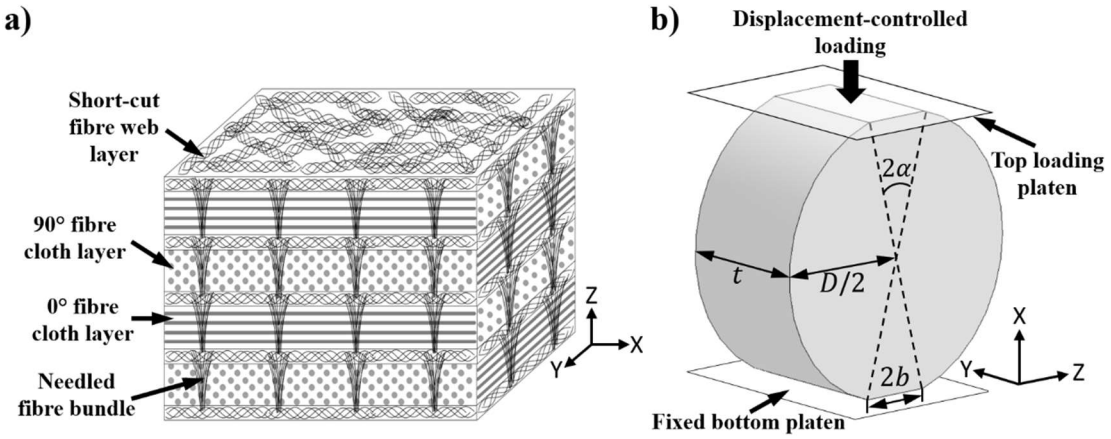

Figure 1. a) Schematic of the 3D needle-punched composite; b) geometry of the FBD specimen. It is noted that displacement-controlled loading was applied to the top loading platen.

The splitting tensile test of flattened Brazilian disc (FBD) specimens[48, 49] was employed to indirectly investigate the C/C composites' tensile behaviour. During the splitting tensile test, the FBD specimen is subjected to a uniform diametral compression (Fig. 1b) [48]; the compression load induces tensile stresses in the centre of the disc specimen in the direction perpendicular to the loading. The tensile stresses then lead to specimen failure by disc splitting. The FBD specimen has two parallel flat ends, which help reduce stress concentration around the loading points that could lead to local cracking. Compared to traditional Brazilian disc samples, the test only requires compression testing platens rather than specialized curved loading fixtures.[48] The geometry of the FBD specimen is shown in Fig. 1b, in which $2\alpha = 30°$, $D = 20$ mm, $t = 10$ mm and $2b = 5.18$ mm [40]. It is noted that quasi-static displacement-controlled loading was applied to the top loading platen (Fig. 1b).

2.2. Finite element model

Finite element (FE) simulations of the splitting tensile test of the C/C composite FBD specimens were performed using Abaqus/Standard (Version 2022).[50] The FE simulations were carried out to understand the effect of the needled fibre bundles and the composite

layered structure on the mechanical behaviour of the C/C composite. First, a mesoscale model of the composite FBD specimen was built, i.e., each layer was explicitly modelled, which included cohesive interfacial behaviour between the layers; in contrast, the needle fibre bundles were modelled using truss elements. Second, a parametric study using various needled fibre bundle configurations was performed to study the role of bundles on the tensile response.

The geometry of the 3D FE model was based on the FBD specimen described in Section 2.1 (Fig. 1b). A thickness of 0.38 mm was used for both the 0° and 90° fibre cloth layers, while for the short-cut fibre web layer, a thickness of 0.22 mm was employed. These layer thicknesses were selected based on scanning electron microscopy (SEM) measurements of the C/C composite experimentally studied elsewhere.[19, 40] The mesh of the C/C composite model is depicted in Fig. 2. Due to symmetry, only a quarter model was constructed to reduce the computational cost associated with a full 3D model (Fig. 2a). Average element sizes of $0.19 \times 0.25 \times 0.27$ mm^3 and $0.22 \times 0.25 \times 0.27$ mm^3 were used for the fibre cloth layer and short-cut fibre web layers, respectively; however, smaller elements were used in some regions near the outer disc edges (Fig 2b). The total number of elements in the model was 84,584. A mesh sensitivity analysis showed that this mesh size was sufficient for convergence. The mesh comprised fully integrated 8-node brick elements (C3D8) and wedge elements (C3D6) for the different composite layers (Fig 2b). Wedge elements were only used in some regions near the outer disc edges (Fig. 2b). To model the needled fibre bundles, 3-node truss elements (T3D3) were used (Fig. 2b), which were embedded in the composite layer elements (host elements) using the embedded region constraint option. In this option, if a node of an embedded element lies within a host element, its translational degrees of freedom are constrained to the interpolated values of the corresponding degrees of freedom of the host element.[50] It is mentioned that some composite layers are not shown in Fig. 2b to illustrate the needled fibre bundles inside the composite specimen. Based on microscopic observations, parallel truss elements were separated by a distance of 1 mm in both X and Y directions (Fig. 2b) and had a diameter of 0.2 mm [40]; however, a parametric study using different distances between the needled fibre bundles was performed and is presented in Section 3.3. Finally, the interface between the different composite layers in the central region (Fig. 2c) was modelled using 3D cohesive elements (COH3D8) with zero thickness (Fig. 2d). Perfectly bonded interfaces between the different composite layers were considered in the

areas near the outer disc edges, where delamination is unlikely, to reduce the computational cost.

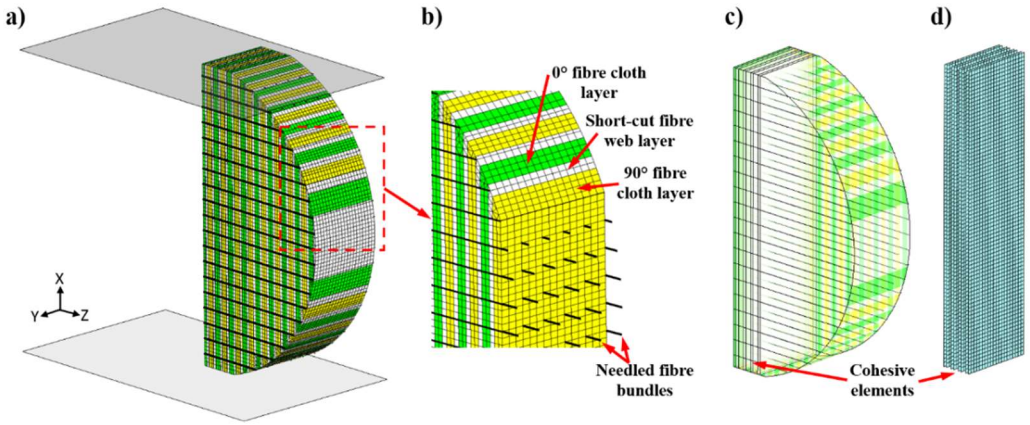

Figure 2. a) Mesh of the FE model of the C/C composite FBD specimen; b) close-up of the mesh near the outer disc edge; c) location of the cohesive elements in the FE model; d) cohesive elements.

The material models and parameters used to capture the mechanical behaviour of the different layers and needled fibre bundles of the C/C composite are presented in the following sections. The material parameters chosen for the FE model were fixed for all the simulations, and the selection of these parameters is also explained in the following sections. Therefore, no variation of the results due to material model parameters is observed in the simulations but rather due to the variation in the number of needled fibre bundles and their distribution, quantified using the volumetric and cross-sectional damage, which is the main scope of this research. As aforementioned, a mesh sensitivity analysis was conducted using four different element sizes with models ranging from ~17,000 to ~131,000 elements. The relative percentage difference R_{pd} of the predicted load at a displacement of 0.07 mm for different mesh sizes was used to assess mesh convergence, which was achieved when R_{pd}< 2%. R_{pd} was calculated as $R_{pd} = 100 \times |F_\mathrm{f} - F_\mathrm{c}|/[(F_\mathrm{f} + F_\mathrm{c})/2]$, where F_f is the predicted load using the finer mesh, and F_c is the predicted load using coarser meshes. The mesh sensitivity analysis showed that convergence was achieved even for the coarser mesh (Fig. 3). This indicates that no variations in the results due to element size are expected for the mesh size used here, for which R_{pd}< 0.1%.

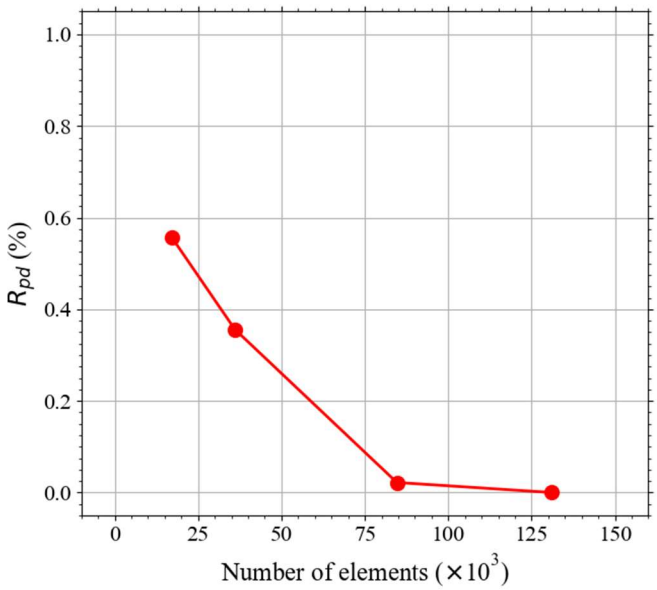

Figure 3. Relative percentage difference R_{pd} of the predicted load at a displacement of 0.07 mm for different mesh sizes.

2.3. Material models

Each unidirectional non-woven fibre cloth layer of the C/C composite was modelled as a transversely isotropic elastic material with damage initiation predicted by the LaRC05 criterion.[50, 51] The LaRC05 criterion is the only built-in damage initiation criterion in Abaqus/Standard (Version 2022) for 3D solid elements.[50] This criterion includes four damage initiation mechanisms: matrix cracking, fibre kinking, fibre splitting, and fibre tension,[50] and requires ten different material input parameters that will be described below. The short-cut fibre web layers and needled fibre bundles were modelled as isotropic and transversely isotropic materials, respectively, with no damage initiation criterion; however, a plasticity model with a single yield stress value was employed to show the onset of damage via the equivalent plastic strain.[50] It is noted that no damage evolution criterion was implemented in the unidirectional non-woven fibre cloth layers since the primary purpose of the FE simulations was to compare the effect of the needled fibre bundles on the stress distribution and damage initiation at the early stages of loading. Finally, cohesive elements were used to model the interfaces between the different composite layers.

2.3.1. Constitutive response and damage initiation criterion of the unidirectional composite layers

Table 1 shows the material properties of the constituents (fibres and matrix),[41, 42, 52] in which the subscripts f and m refer to the fibre and matrix, respectively. The subscript 1 refers to the longitudinal direction of the fibre, while subscripts 2 and 3 refer to the transverse directions of the fibre. Finally, the superscripts T and C refer to the tensile and compressive strengths, respectively.

Table 1. Material properties of the constituents of the C/C composite.[41, 42, 52, 53]

Properties	T700 carbon fibre	HTS40 carbon fibre	Carbon matrix
Elastic modulus E (GPa)	$E_{f11} = 237$ $E_{f22} = E_{f33} = 15.8$	$E_{f11} = 239$	$E_m = 7.76$
Shear modulus G (GPa)	$G_{f12} = G_{f13} = 23$ $G_{f23} = 15$	–	$G_m = 3.38$
Poisson's ratio ν $(-)$	$\nu_{f12} = \nu_{f13} = 0.27$ $\nu_{f23} = 0.3$	–	$\nu_m = 0.2$
Tensile strength σ^T (MPa)	$\sigma_{f11} = 5300$	$\sigma_{f11} = 4900$	$\sigma_m^T = 12.3$
Compressive strength σ^C (MPa)	–	–	$\sigma_m^C = 57$
Shear strength τ (MPa)	–	–	$\tau_m = 16$

The effective elastic properties and strengths of non-woven fibre cloth unidirectional composite layers can be estimated using the micromechanics equations from Chamis.[54] This set of equations was selected because of its simplicity in calculating transverse properties requiring only the fibre volume fraction in addition to the constituent's material properties and being successfully used to calculate the properties of C/C composites non-woven cloth unidirectional layers.[42, 55] The micromechanics equations are shown in Eq. (1) and Eq. (2), respectively:

$$E_{l11} = V_f E_{l11} + (1 - V_f)E_m \quad (1)$$

$$E_{l2} = E_{l3} = E_m/(1 - \sqrt{V_f}(1 - E_m/E_{f2}))$$

$$G_{l12} = G_{l13} = G_m/(1 - \sqrt{V_f}(1 - G_m/G_{f1}))$$

$$G_{l23} = G_m/(1 - \sqrt{V_f}(1 - G_m/G_{f23}))$$

$$\nu_{l12} = \nu_{l13} = V_f \nu_{f12} + (1 - V_f)\nu_m$$

$$X_T = V_f \sigma_{f11} \quad (2)$$

$$Y_T = (1 - (\sqrt{V_f} - V_f)(1 - E_m/E_{f22}))\sigma_m^T$$

$$Y_C = (1 - (\sqrt{V_f} - V_f)(1 - E_m/E_{f22}))\sigma_m^C$$

$$S_L = (1 - (\sqrt{V_f} - V_f)(1 - G_m/G_{f12}))\tau_m$$

where V_f is the fibre volume fraction, the subscript l refers to the composite layer, X_T and Y_T are the longitudinal and transverse tensile strengths, Y_C is the transverse compressive strength, and S_L is the longitudinal shear strength of the non-woven composite unidirectional layers. A double-subscript notation was used in Eqs. (1) and (2) and the material properties in Tables 1 and 2 to be consistent with the notation used in the equations developed by Chamis.[54] It is, however, clarified that, for instance, E_{f11} represents the elastic modulus in the 1-direction.

The effective elastic properties and strengths of the non-woven composite unidirectional layers shown in Table 2 were estimated using Eq. (1) and Eq. (2), the mechanical properties in Table 1 and V_f=0.3. Due to carbon fibre mechanical property degradation during heat treatment in C/C composite manufacturing, a decrease in E_{f11} and σ_{f11} of up to 30% and 50%, respectively, is expected.[56] Therefore, E_{f11} and σ_{f11} were reduced to 166 GPa and 2650 MPa, respectively; these values were used in Eq. (1) and Eq. (2) to calculate the properties for the simulations shown in Table 2. In contrast, the transverse properties should not degrade since the matrix properties dominate them.[41] Additionally, in Table 2, ν_{l23} was obtained from Xie et al.[42] It has been reported that direct in-situ testing of the longitudinal compressive strength X_C is difficult; however, some studies measured X_C as ~40-60% of the tensile strength X_T.[41] Here, X_C was taken as 50% of the X_T value, that is, X_C=0.5X_T.[41] Similarly, the

transverse shear strength S_T is a material property that is difficult to measure experimentally; however, Davila et al.[57] developed a method to estimate it as S_T=$0.378Y_C$,[57] based on the assumption that the angle of the fracture plane α_0 of a unidirectional composite loaded in transverse compression is typically ~53°.[58] It has been reported that α_0 is typically in the range of 51°-55° for carbon composites.[51]

Table 2. Effective material properties for the different layers and needled fibre bundles of the C/C composite, which were estimated using micromechanics formulas.

	Properties	Non-woven cloth layer	Short-cut fibre layer	Needled fibre bundle
Elastic properties	Elastic modulus (GPa)	$E_{l11} = 55.2$ $E_{l22} = E_{l33} = 10.76$	$E = 22.7$	$E_1 = 39.5$
	Shear modulus (GPa)	$G_{l12} = G_{l13} = 6.34$ $G_{l23} = 5.87$	$G = 8.1$	$G_{12} = G_{13} = 4.6$ $G_{23} = 4.2$
	Poisson's ratio (-)	$\nu_{l12} = \nu_{l13} = 0.21$ $\nu_{l23} = 0.23$	$\nu = 0.4$	$\nu_{12} = \nu_{13} = 0.21$ $\nu_{23} = 0.23$
Strength	Tensile strength (MPa)	$X_T = 795, Y_T = 10.75$	–	–
	Compressive strength (MPa)	$X_C = 397.5, Y_C = 49.8$	–	–
	Shear strength (MPa)	$S_L = 12.6, S_T = 18.8$	–	–
	Initial yield stress (MPa)	–	$\sigma_y = 71.6$	$\sigma_y = 71.6$

The LarC05 damage initiation criterion was used to model the damage initiation of the composite unidirectional layers. This criterion requires the longitudinal and transverse strengths X_T, X_C, Y_T, Y_C, S_L, S_T as input parameters. In addition, it requires the following input parameters, which were obtained from Gouskos and Iannucci[59] and are provided in Table 3: the fracture plane angle for pure compression α_0, the initial misalignment angle φ_0, and the longitudinal and transverse shear friction coefficients η_L and η_T. Regarding the values in Table 3, the selection of α_0 was based on the typical angle of the fracture plane of carbon composites, as explained in detail before. φ_0 is a material property that represents

initial microstructural defects that can trigger kink-band formation.[60] Based on the literature,[59, 61] a small value of φ_0=2.544° was used here. The selection of η_T was based on the equation $\eta_T = -1/\tan 2\alpha_0$,[61] while the value of η_L was taken from the literature.[59]

The output variables related to the damage initiation mechanisms of the LarC05 criterion are LARCMCCRT (matrix cracking), LARCFKCRT (fibre kinking), LARCFSCRT (fibre splitting) and LARCFTCRT (fibre tension). A value equal to or greater than 1.0 in any output variable indicates that the particular damage initiation criterion has been satisfied.[50]

Table 3. LarC05 damage criterion parameters.

Properties	Non-woven cloth layer
Fracture plane angle (°)	$\alpha_0 = 53$
Misalignment angle (°)	$\varphi_0 = 2.544$
Longitudinal shear friction coefficient	$\eta_L = 0.082$
Transverse shear friction coefficient	$\eta_T = 0.287$

2.3.2. Constitutive response of the short-cut fibre composite layers and needled fibre bundles

The constitutive behaviour of the short-cut fibre web layers and needled fibre bundles was modelled using the micromechanics formulas in Eq. (3), the properties in Table 1, and V_f=0.2. This value of V_f was selected by assuming that most of the fibres in the needled fibre bundles came from the short-cut fibre web layers, considering that the short-cut fibres are introduced into the preform during the needle-punching process;[62] thus, both the short-cut fibre web layers and needled fibre bundles had the same V_f. Furthermore, compared to the more densely-packed fibres in the non-woven fibre cloth unidirectional layers, it was assumed that the short-cut fibre web layers had a lower V_f of 20%, which has been employed in other investigations.[41, 63] Short-cut fibre web layers and needled fibre bundles were considered short-fibre composites; however, while the needled fibre bundles were considered unidirectional short-fibre composites, for the short-cut fibre web layers the random orientation of the fibres was also considered. The Halpin-Tsai model[64-67] was used to estimate the elastic properties of a unidirectional short-fibre composite with circular fibres:

$$\frac{E_1}{E_m}=\frac{1+(2L/d)\eta_1 V_f}{1-\eta_1 V_f},\frac{E_2}{E_m}=\frac{1+2\eta_2 V_f}{1-\eta_2 V_f},\frac{G_{12}}{G_m}=\frac{1+\eta_{12} V_f}{1-\eta_{12} V_f},\frac{G_{23}}{G_m}=\frac{1+\zeta\eta_{23} V_f}{1-\eta_{23} V_f},\quad \nu_{12}=\nu_{f12}V_f+\nu_m V_m \qquad (3)$$

where

$$\eta_1=\frac{E_{f1}\ /E_m-1}{E_{f11}/E_m+(2L/d)},\eta_2=\frac{E_{f11}/E_m-1}{E_{f1}\ /E_m+2},\eta_{12}=\frac{G_{f12}/G_m-1}{G_{f12}/G_m+1},\eta_{23}=\frac{G_{f12}/G_m-1}{G_{f1}\ /G_m+1},\zeta=\frac{1+\nu_m}{3-\nu_m-\nu_m^2}$$

In Eq. (3), L is the length of the fibre estimated as 6 mm while d=7 μm is the diameter of the fibre. As aforementioned, reduced fibre tensile properties (E_{f11}=168 GPa and σ_{f11}=2450 MPa) were used in Eq. (3). For the short-cut fibre web layers, E_1 and E_2 from Eq. (3) were used in the following formulas (Eq. (4))[66] to estimate the elastic properties of the randomly-oriented composite:

$$E=(3/8)E_1+(5/8)E_2 \qquad (4)$$

$$G=(1/8)E_1+(1/4)E_2$$

$$\nu=E/2G-1$$

In addition, the initial yield stress of σ_y = 71.6 MPa was used[68] for both short-cut fibre web layers and needled fibre bundles. The estimated mechanical properties of short-cut fibre web layers and needled fibre bundles, using Eq. (4) and Eq. (3), respectively, are shown in Table 2.

2.3.3. Constitutive response of the cohesive elements

The 3D cohesive elements (COH3D8) used to model the interface between the different composite layers followed a bilinear traction-separation constitutive law,[50] which assumes an initial linear elastic behaviour, that is, under external loading, the initial traction force of the cohesive interface material increases linearly with the displacement caused by the external force.[69] Since zero-thickness cohesive elements were used, the interface stiffness in the normal direction K_n and transverse directions K_s and K_t must be defined to describe the elastic response of the material. Following the initial elastic response, material damage starts

to occur once a damage initiation criterion is met. Here, the damage initiation of the cohesive elements is assumed to occur when a quadratic interaction function involving the normal traction t_n and the shear tractions t_s and t_t reaches a value of 1, as follows:

$$\left(\frac{t_n}{t_n^0}\right)^2 + \left(\frac{t_s}{t_s^0}\right)^2 + \left(\frac{t_t}{t_t^0}\right)^2 = 1 \qquad (5)$$

where t_n^0 is the normal strength, and t_s^0 and t_t^0 are the shear strengths. t_n^0 represents the peak value of the nominal stress (traction) when the deformation is purely normal to the interface, while t_s^0 and t_t^0 represent the peak values when the deformation is in the first or second shear direction, respectively (Fig. 4a).[50] The corresponding separation (the relative displacements between the top and bottom faces of the cohesive element) of the normal and shear tractions are denoted by δ_n, δ_s and δ_t, respectively. The normal and shear separations at the peak strengths are denoted by δ_n^0, δ_s^0 and δ_t^0, respectively (Fig. 4a).

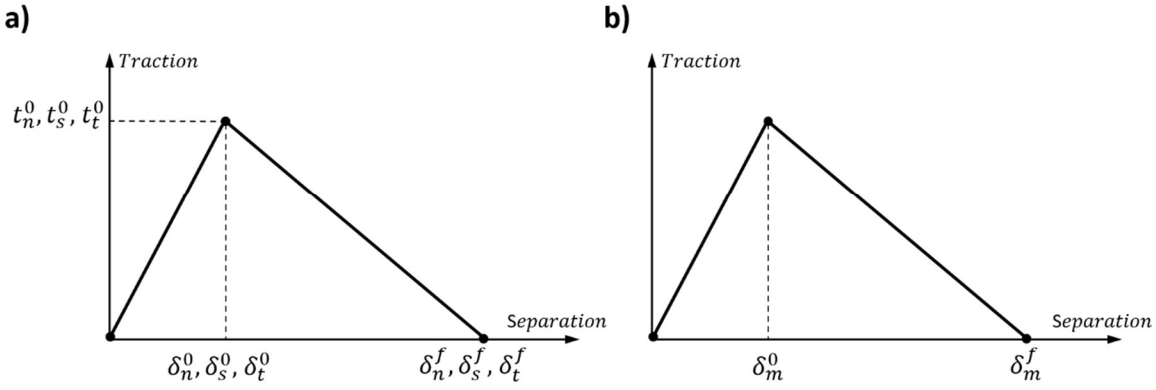

Figure 4. a) Bilinear traction-separation response of the cohesive elements; b) linear damage evolution (softening) based on effective displacement.

Following damage initiation, damage evolution in the cohesive elements will result in linear material softening; the damage then progressively extends, resulting in a linear reduction of the traction force with further displacement due to stiffness degradation. Here, linear softening was used for the damage evolution law of the cohesive elements using the effective displacement at complete failure δ_m^f, relative to the effective displacement at damage initiation δ_m^0 (Fig. 4b).[50] The effective displacement δ_m, employed to describe the

damage evolution under a combination of normal and shear deformation across the interface (cohesive element) is defined as[50]:

$$\delta_m = \sqrt{\delta_n^2 + \delta_s^2 + \delta_t^2} \quad (6)$$

For linear softening, the evolution of the scalar damage variable D is defined as[70]:

$$D = \frac{\delta_m^f(\delta_m^{max} - \delta_m^0)}{\delta_m^{max}\left(\delta_m^f - \delta_m^0\right)} \quad (7)$$

where δ_m^{max} is the maximum value of δ_m attained during the loading history.[50] D represents the overall damage in the material and initially has a value of 0 at the initiation of damage ($\delta_m = \delta_m^0$) and then increases monotonically with further loading up to a value of 1 at complete failure ($\delta_m = \delta_m^f$).[50] A large value of δ_m^f (1 mm) was used in the simulations since the primary purpose of the cohesive element layers was to account for stiffness degradation at the interface compared to perfectly bonded interfaces while avoiding any premature delamination that could occur, considering that the needled fibre bundles modelled using truss elements cannot capture the deflection of delamination cracks, which were observed experimentally at large displacements.[40] Table 4 shows the material parameters of the cohesive interface used between the different composite layers. The interface stiffness values (K_n, K_s, K_t) in Table 4 were chosen based on similar values found in the literature for carbon matrix composites, which ranged from 5×10^4 to 10^6.[68, 71] The normal and shear strength values (t_n^0, t_s^0, t_t^0) in Table 4 were selected based on values found in the literature for C/C composites.[72, 73]

Table 4. Material properties and cohesive element parameters for the interface between the different composite layers.

Properties	
K_n, K_s, K_t (N/mm^3)	10^5
t_n^0 (MPa)	12
t_s^0, t_t^0 (MPa)	6

3. Results and discussion

3.1. Experimental validation of the FE model

Fig. 5 compares the predicted load-displacement curve of the needle-punched C/C composite FBD specimen with the average experimental load-displacement curve with standard deviation (shaded area) obtained from specimens subjected to the splitting tensile test.[40] It is mentioned that in Flores-Johnson et al.,[40] three FBD specimens were tested, and good repeatability was observed based on the obtained load-displacement curves and the measured values of the peak load (11.84 ± 0.46 N) and the displacement at peak load (0.17 ± 0.02 mm).[40] It can be seen in Fig. 5 that the FE model predicts the load-displacement curve well; however, it slightly overestimates the stiffness of the sample (indicated by the slope of the load-displacement curve). For instance, the predicted load at a displacement of 0.07 mm is 7.6% higher than the average experimental load. This observation is explained by the numerical model not considering voids and pre-existing cracks, which contribute to the stiffness reduction. In addition, the FE model does not consider localised damage evolution occurring at the early stages of loading. Furthermore, the model is not designed to predict the load-displacement curves for displacements > 0.07 mm, in which large inelastic deformation occurs, as a damage evolution model was not implemented for the 0° and 90° fibre layers. As mentioned, the FE models aim to show the effect of the needled fibre bundles on the mechanical response at low displacements at the early stages of loading. Fig. 5 also shows the predicted load-displacement curve of a C/C composite FBD specimen without needled fibre bundles, in which the truss elements have been removed from the simulation. Although it can be seen that the curve predicted by the FE model with needled fibre bundles is slightly higher than the curve of the model without needled fibre bundles, it is evident that the needled fibre bundles do not significantly affect the predicted load-displacement behaviour at low displacements at the early stages of loading. Notwithstanding, the needled fibre bundles greatly influence the strain distribution in the central region of the specimen, as will be discussed below.

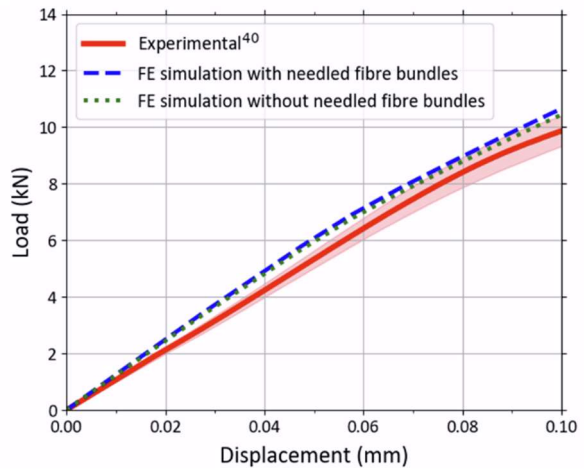

Figure 5. Comparison of the average experimental load-displacement curve[40] with standard deviation (shaded area) with the predicted load-displacement curve of the C/C composite FBD specimen (with and without needled fibre bundles) subjected to the splitting tensile test.

Fig. 6a shows the experimental DIC contour of the strain in the Z direction (ε_Z),[40] which is normal to the compressive loading direction (X direction), at a displacement of 0.07 mm corresponding to ~60% of the average peak load), along with the corresponding predicted ε_Z contour using the FE model of the C/C composite FBD specimen (with needled fibre bundles) subjected to the splitting tensile test. It is noted that the FE model has been mirrored with respect to the symmetry plane to show the entire specimen. It can be seen that the FE model can accurately predict the location of the highest tensile strains occurring in the 0° fibre layers (in red colour) and the highest compressive strains at the flat ends of the specimen (in blue colour). Similarly, Fig. 6b shows the DIC contour of the strain in the X direction (ε_X),[40] which is parallel to the compressive loading direction, along with the predicted contour, where it can be seen that the predicted highest compressive strains in the central region agree with the experimental results.

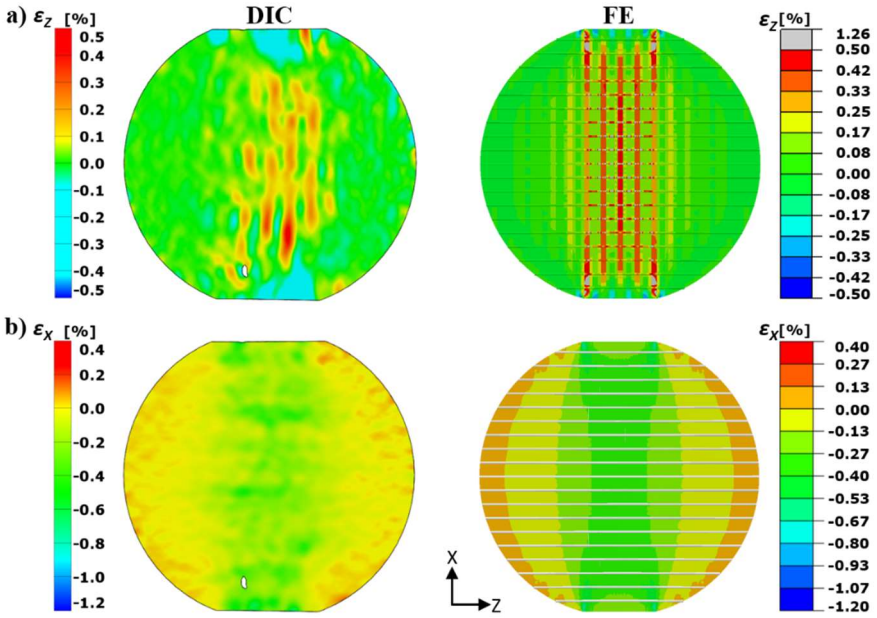

Figure 6. Comparison of experimental DIC strain contours[40] with the predicted contours from the FE model of the C/C composite with needled fibre bundles subjected to the splitting tensile test: a) strain ε_Z (normal to the applied load); b) strain ε_X (parallel to the applied load).

3.2. Numerical analysis of the splitting tensile behaviour and damage of C/C composites with and without needled fibre bundles

Fig. 7a shows the predicted strain ε_Z at a displacement of 0.07 mm for the FE model with needled fibre bundles. It can be seen that the needled fibre bundles exhibit high levels of tensile strain, which enables more global distribution of the strain ε_Z, which in turn reduces the area with high strain levels (in grey colour) in the middle of the specimen, as seen in the cross-section. It is noted that the cross-section has been mirrored with respect to the symmetry plane to show the entire specimen. In contrast, the FE model without needled fibre bundles (Fig. 7b) exhibits a larger area of high tensile strain levels, which are visible on the outer surface at the 0° fibre layer located in the centre of the specimen (in grey colour). Fig. 7c shows the predicted stress in the Z direction (σ_Z), normal to the applied load, for the FE model with needled fibre bundles. It can be seen that the tensile stress in the needled fibre bundles is high, which reduces the stress levels in other parts of the composite. In contrast, a larger area of high tensile stress is observed in the FE model without needled fibre bundles (Fig. 7d). Fig. 7e and 7f show the contours of the damage variable SDEG for the cohesive elements of the FE models with and without needled fibre bundles, respectively. For the composite with needled fibre bundles, more global distribution of the damage in the cohesive

elements (larger damaged area) is observed (Fig. 7e) compared to the composite without needled fibre bundles (Fig. 7f). In addition, damage in the cohesive elements is not observed in the central region of the specimen with needled fibre bundles (Fig. 7e). In contrast, areas with higher damage levels (in grey colour) are observed for the composite without needled fibre bundles (Fig. 7f). Moreover, damage in the cohesive elements in the middle of the specimen is observed for the composite without needled fibre bundles (Fig. 7f).

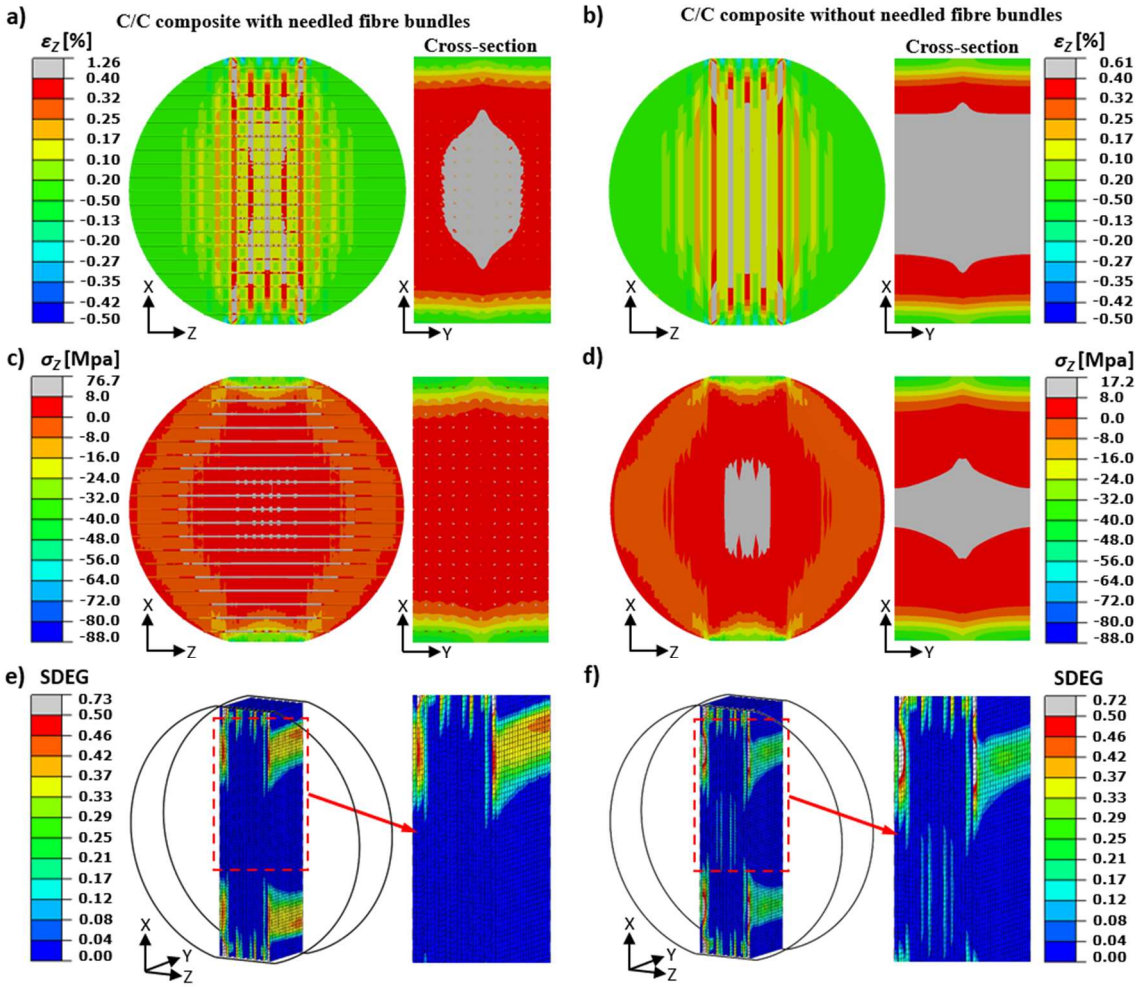

Figure 7. Comparison of the predicted contours of the strain ε_Z (normal to the applied load) from the FE models of the C/C composite: a) with needled fibre bundles, b) without needled fibre bundles. Comparison of the predicted contours of the stress σ_Z: c) with needled fibre bundles, d) without needled fibre bundles. Comparison of the predicted contours of the damage variable (SDEG) of the cohesive elements: e) with needled fibre bundles, f) without needled fibre bundles.

Figs. 8a and 8b show the contours of the LarC05 criterion output variables for the FE models with and without needled fibre bundles, respectively, at a displacement of 0.07 mm. The output variables include LARCMCCRT (matrix cracking), LARCFKCRT (fibre kinking), and LARCFSCRT (fibre splitting). In the contours, the regions where the damage initiation mechanisms have been met (output variable > 1.0) are shown in red and brown colour, while the areas where the criterion has just been met or is close to being met ($0.5 \leq$ output variable ≤ 1.0) are shown in orange colour. It is noted that the short-cut fibre web layers appear in white colour (not showing any value) as the LarC05 criterion can only be used for unidirectional fibre-reinforced composites. It is also noted that the fibre tension initiation mechanism (LARCFTCRT) is not presented since this criterion was not met in any of the simulations.

For the predicted matrix cracking initiation criterion (LARCMCCRT), it can be seen in Fig. 8 that there is matrix cracking in the regions near the flat ends in both cases (with and without needled fibre bundles). However, the matrix cracking area in the specimen's centre is much more significant for the model without needle fibre bundles. For the fibre kinking criterion (LARCFKCRT), the regions in which this type of damage is observed are very similar in both cases (with and without needled fibre bundles), as depicted in Fig. 8. These areas are observed in the 0° fibre layers near the flat edges, which is explained by the high levels of compressive strain ε_X observed in those locations (Fig. 6b). Finally, for the fibre splitting criterion (LARCFSCRT), it can be seen in Fig. 8 that the regions where this criterion has been met (i.e., the 0° fibre layers) are similar in both cases; however, it can be seen that in the central region of the model without the needled fibre bundles, the criterion for the splitting damage has been fully met in three 0° fibre layers (red colour). In contrast, the criterion has only been partially met in the model with needled fibre bundles.

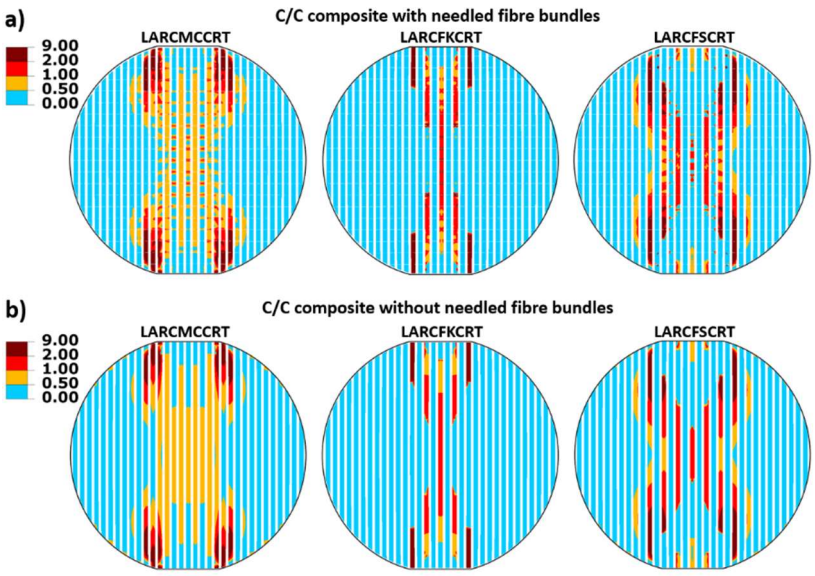

Figure 8. Comparison of the predicted contours of the LaRC05 criterion output variables, including LARCMCCRT (matrix cracking), LARCFKCRT (fibre kinking), and LARCFSCRT (fibre splitting): a) C/C composite model with needled fibre bundles; b) C/C composite model without needled fibre bundles.

3.3. Influence of the needled fibre bundle configuration on the damage of C/C composites with and without needled fibre bundles

The FE simulation results in the previous section showed the crucial role that needled fibre bundles play in the structural performance of the C/C composites as they redistribute the deformation in the specimen, producing less stress concentration. To further understand the influence of the needled fibre bundle configuration on the mechanical properties, two additional cases were numerically evaluated (N2 and N0.5), as shown in Fig. 9a, i.e., the distance between the needled fibre bundles was varied (and thus the number of bundles); L_N indicates the shortest distance between the bundles. In Fig. 9a, N1 corresponds to the configuration of the C/C composite specimens tested experimentally[40]. Fig. 9b shows the contours of the LarC05 criterion output variable LARCMCCRT (matrix cracking) for FE models without needled fibre bundles (NN) and with various needled fibre bundle configurations (Fig. 9a) at a displacement of 0.07 mm. In all cases, the left image shows the external specimen surface, while the right image shows the cross-section in the middle of the specimen. It can be seen in the central region of the specimen (Fig. 9b) that the area where the matrix cracking has occurred or is nearly occurring (output variable ≥ 0.5) reduces with

the reduction of the distance between the needled fibre bundles (increase in the number of bundles).

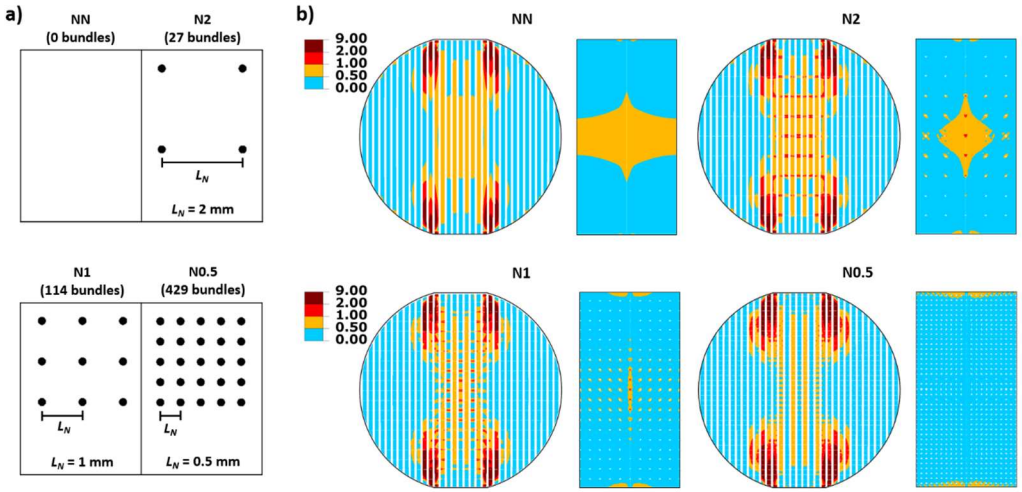

Figure 9. a) Needled fibre bundle configurations for the numerical study. b) Comparison of the predicted contours of the LaRC05 criterion output variable LARCMCCRT (matrix cracking) for C/C composite models without needled fibre bundles (NN) and with various needled fibre bundle configurations.

The volumetric damage was calculated as the volume of damaged elements (output variable > 1.0) divided by the total volume of the specimen. In contrast, the cross-sectional damage was calculated as the damaged cross-sectional area in the middle of the specimen divided by the total area of the cross-section. Both the volumetric damage and the cross-sectional damage were plotted against the number of needled fibre bundles of each configuration for a displacement of 0.07 mm (Fig. 10) to quantify the matrix damage shown in Fig. 9b. It can be seen in Fig. 10 that there is a reduction in the volumetric and cross-sectional damage with the increase in the number of bundles, which follows a somewhat negative linear relationship from 0 to 114 bundles. When the number of bundles is increased from 114 to 429 (configuration N0.5), the volumetric damage is further reduced; however, the reduction is not as significant considering the large increase in the number of bundles. In contrast, Fig. 10 shows that increasing the needled fibre bundles from 114 to 429 significantly reduced the cross-sectional damage area from 21.1% to 5.4%.

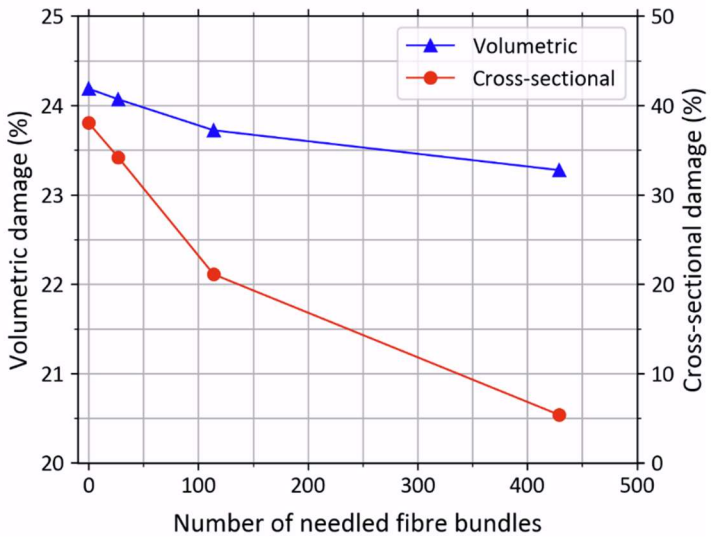

Figure 10. Volumetric and cross-sectional damage of the FE models without needled fibre bundles (NN) and with various needled fibre bundle configurations (see Figure 9).

3.4. Discussion

As mentioned, the FE simulations revealed the critical importance of the needled fibre bundles in the structural performance of the C/C composites, redistributing the deformation in the specimen more globally, resulting in less stress concentration. The results also showed that increasing the number of needled fibre bundles reduces the extension of the damage in the matrix, which could improve mechanical performance and avoid catastrophic failure by sudden delamination.

It is acknowledged, however, that the FE model presented here is limited by the assumption that no damage evolution occurs at low displacements at the early stages of loading. The lack of microscopic features, such as voids and defects, also limits the FE model. Therefore, it is recommended that future work uses an FE model that includes a damage evolution criterion coupled with the LarC05 damage initiation criterion to predict and analyse crack propagation at large displacements.[74] Furthermore, it is acknowledged that a model that considers porosity and pre-existing damage could provide more accurate results, particularly in the inelastic response of the C/C composites; thus, an FE model that includes these characteristics is recommended when microstructural features are important for specific numerical studies.[75] However, it should be considered that a model that explicitly considers small features, such as needled fibre bundles, voids and cracks, takes more time to build and requires extensive computational resources due to the large number of elements needed to

capture all the composite features.[3] It is also recommended to include the anisotropy of the matrix in the FE model material properties, which could result from specific manufacturing processes.[76] Related to the previous recommendation, a parametric study using different material properties for the matrix and interface, resulting from different manufacturing process parameters[77] or various manufacturing processes, could be of interest to improve the fabrication of C/C composites. For this purpose, a computational methodology evaluating a large number of numerical simulations to understand each material parameter's range and its effect on results variations is recommended if computationally efficient FE models are available.[78] Finally, further studies are recommended to investigate the effect of the configuration and number of bundles on the mechanical performance of C/C composites.

It is concluded that the FE model presented here can be used to investigate the splitting tensile behaviour of needle-punched C/C composites for low displacements, and the approach employed in these simulations could be used to model the macroscopic mechanical behaviour of other needle-punched composites.

4. Conclusions

This work numerically investigated the splitting tensile strength of needle-punched C/C composites through the diametral loading of flattened Brazilian discs (FBD). The finite element (FE) simulations demonstrated the capability of the model to predict the splitting tensile behaviour of the needle-punched C/C composites at the early stages of loading, including the prediction of the regions with the highest compressive and tensile strains observed experimentally. The FE simulations of FBD subjected to diametral loading showed that the needled fibre bundles play a crucial role in the tensile performance of the C/C composites by carrying tensile stresses perpendicular to the loading direction and reducing the levels of localised deformation in the central region of the specimen at the early stages of loading. In addition, the damage initiation criterion showed that when the needle fibre bundles are included in the FE simulation, the extension of damaged areas (matrix cracking) is less than in the simulations without needled fibre bundles. Furthermore, the numerical results also showed that increasing the number of the needled fibre bundles further reduced the extension of the damage in the matrix.

Acknowledgements

The authors thank C. Yang for providing the material, and O. Muránsky for his assistance with the modelling work and experimental results used for the model validation.

Declaration of conflicting interests

The author(s) declared no potential conflicts of interest with respect to the research, authorship, and/or publication of this article.

Funding

The authors gratefully acknowledge the Australian Institute of Nuclear Science and Engineering (AINSE) for providing financial support to J. Townsend through the Honours Scholarship.

Data availability statement

The datasets generated during and/or analysed during the current study are available from the corresponding author on reasonable request.

References

1. Windhorst T and Blount G (1997) Carbon-carbon composites: a summary of recent developments and applications. *Mater Des* 18: 11-15. https://doi.org/10.1016/S0261-3069(97)00024-1.
2. Manocha LM (2003) High performance carbon-carbon composites. *Sadhana* 28: 349-358. https://doi.org/10.1007/BF02717143.
3. Zahid M, Sharma R, Bhagat AR and Karra P (2021) Image-based numerical modeling for the effective thermo-elastic property of 4D carbon/carbon composite at high temperatures. *Compos Struct* 267: 113881. https://doi.org/10.1016/j.compstruct.2021.113881.
4. Zahid M and Sharma R (2020) Thermal shock resistance of 4D-inplane carbon/carbon composite based on micro-structurally informed effective properties. *Mater Today Commun* 25: 101637. https://doi.org/10.1016/j.mtcomm.2020.101637.
5. Murali T, Murad MS, Bakir M and Asmatulu R (2024) PAN-based fiber-reinforced carbon-carbon composites for improved fire retardancy and thermal and electrical conductivities for harsh environments. *J Compos Mater* 58: 1751-1768. https://doi.org/10.1177/00219983241246610.
6. Zaldivar R, Martinez A, Elhessen R, et al. (2023) The effect of heat-treatment temperature (HTT) on the carbon matrix development of both polyarylacetylene-and phenolic-derived carbon–Carbon (C/C) composites. *J Compos Mater* 57: 3649-3662. https://doi.org/10.1177/00219983231191165.
7. Qinlu Y, Yulong L, Hejun L, et al. (2008) Quasi-static and dynamic compressive fracture behavior of carbon/carbon composites. *Carbon* 46: 699-703. https://doi.org/10.1016/j.carbon.2008.01.031.

8. Wei K, Shi H, Li J and Tang M (2022) A new progressive damage model for predicting the tensile behavior of the three-dimensional woven carbon/carbon composites using micromechanics method. *Int J Damage Mech* 31: 294-322. https://doi.org/10.1177/10567895211035496.
9. Jia J, Ju J, Liu S and Ji G (2021) Preparation and mechanical properties of C/C composites reinforced with arrayed SiC columnar pins. *Ceram Int* 47: 24262-24269. https://doi.org/10.1016/j.ceramint.2021.05.137.
10. Bogachev E and Elakov A (2022) Organomorphic carbon–carbon composite for hot pressing molds. *Int J Appl Ceram Technol* 19: 101-107. https://doi.org/10.1111/ijac.13813.
11. Tan Z, Zhang X, Ruan J, et al. (2021) Synthesis, structure, and properties of carbon/carbon composites artificial rib for chest wall reconstruction. *Sci Rep* 11: 11285. https://doi.org/10.1038/s41598-021-90951-8.
12. Dhami TL and Bahl OP (2005) Challenges in Carbon/Carbon Composites Technologies. *Carbon Sci* 6: 148-157. https://koreascience.kr/article/JAKO200522463505946.pdf.
13. Reiner J, Narain D, Zhang P, et al. (2023) Progressive fracture testing of Carbon-Carbon composites. *Ceram Int* 49: 6451-6458. https://doi.org/10.1016/j.ceramint.2022.10.198.
14. Popp G, Gruber U, Boder H and Janssen K (1984) Graphite and Carbon/Carbon Components for Hot Gas Ducts. In: Specialists' Meeting on Heat Exchanging Components of Gas-Cooled Reactors, International Atomic Energy Agency. Düsseldorf, Germany, April 16-19, 1984, Available online: https://www.osti.gov/etdeweb/servlets/purl/20111125 (accessed on 25 October 2022).
15. Venugopalan R, Sathiyamoorthy D and Tyagi AK (2012) Development of Carbon / Carbon Composites for Nuclear Reactor Applications. *BARC Newsletter* March-April: 16-20. https://www.barc.gov.in/barc_nl/2012/20120304.pdf.
16. Locatelli G, Mancini M and Todeschini N (2013) Generation IV nuclear reactors: Current status and future prospects. *Energy Policy* 61: 1503-1520. https://doi.org/10.1016/j.enpol.2013.06.101.
17. David P. 13 - Carbon/carbon materials for Generation IV nuclear reactors. In: Yvon P (ed) *Structural Materials for Generation IV Nuclear Reactors*. Woodhead Publishing, 2017, pp.471-493.
18. Eto M, Konishi T, Shibata T and Sumita J (2011) Research and developments on application of carbon-carbon composite to HTGR/VHTR in Japan. *IOP Conf Ser: Mater Sci Eng* 18: 162003. https://doi.org/10.1088/1757-899X/18/16/162003.
19. Wang Z, Muránsky O, Zhu H, et al. (2022) Impact of pre-existing crystal lattice defects on the accumulation of irradiation-induced damage in a C/C composite. *J Nucl Mater* 564: 153684. https://doi.org/10.1016/j.jnucmat.2022.153684.
20. Corwin WR, Burchell TD, Katoh Y, et al. Generation IV Reactors Integrated Materials Technology Program Plan: Focus on Very High Temperature Reactor Materials. Report. United States, August 2008. https://doi.org/10.2172/951084.
21. Song P, Xiao P, Liu J and Wang YH (2019) The inspection of coating thickness uniformity of SiC-coated carbon-carbon (C/C) composites by laser-induced thermal-wave imaging. *Carbon* 147: 348-356. https://doi.org/10.1016/j.carbon.2019.03.015.
22. Wang W, Fu Q, Sun J, et al. (2022) The mechanical and repair behavior of damaged carbon/carbon composites. 48: 22759-22766. https://doi.org/10.1016/j.ceramint.2022.04.076.
23. Zhang J and An P (2019) Modeling quasi-3D needle-punched C/C composites using a linear simplification representative volume element model. *AIP Adv* 9: 035344. https://doi.org/10.1063/1.5068727.
24. Zhou W, Wente T, Liu D, et al. (2020) A comparative study of a quasi 3D woven composite with UD and 2D woven laminates. *Compos Part A* 139: 106139. https://doi.org/10.1016/j.compositesa.2020.106139.
25. Chen X, Chen L, Zhang C, et al. (2016) Three-dimensional needle-punching for composites – A review. *Compos Part A* 85: 12-30. https://doi.org/10.1016/j.compositesa.2016.03.004.
26. Qingliang S, Guangmeng Y, Caixiang X, et al. (2022) Control of multi-scale cracking for improvement of the reliability of carbon/carbon composites via design of interlaminar stress. *Compos Struct* 297: 115985. https://doi.org/10.1016/j.compstruct.2022.115985.
27. Ma Z, Ma W, Man R, et al. (2023) Effect of fabric structural stability on the tensile property of bidirectional angle-interlock woven composites. *Int J Damage Mech* 32: 989-1007. https://doi.org/10.1177/10567895231181608.
28. Patnaik PK, Swain PTR, Mishra SK, et al. (2020) Recent developments on characterization of needle-punched nonwoven fabric reinforced polymer composites – A review. *Mater Today: Proc* 26: 466-470. https://doi.org/10.1016/j.matpr.2019.12.086.
29. Lawrence BD, Bogetti TA and Emerson RP (2015) Processing and Characterization of Needled Carbon Composites. In: Proceedings of the 2015 Composites and Advanced Materials Expo (CAMX). Dallas, USA, October 26-29, 2015, Available online: https://apps.dtic.mil/sti/pdfs/AD1000526.pdf (accessed on 27 October 2022).

30. Han M, Wang Z, Zhang X, et al. (2024) Short-term oxidation and residual compression properties of needle-punched carbon/carbon composites. *J Compos Mater* 58: 1353-1362. https://doi.org/10.1177/00219983241241119.
31. Zhang J, Luo R, Xiang Q and Yang C (2011) Compressive fracture behavior of 3D needle-punched carbon/carbon composites. *Mater Sci Eng A* 528: 5002-5006. https://doi.org/10.1016/j.msea.2011.03.055.
32. Li D and Wong LNY (2013) The Brazilian Disc Test for Rock Mechanics Applications: Review and New Insights. *Rock Mech Rock Eng* 46: 269-287. https://doi.org/10.1007/s00603-012-0257-7.
33. Yin T, Yang Z, Wu Y, et al. (2022) Experimental investigation on the effect of open fire on the tensile properties and damage evolution behavior of granite. *Int J Damage Mech* 31: 1139-1164. https://doi.org/10.1177/10567895221092168.
34. Smolin IY, Zimina VA, Sablina TY, et al. (2022) Experimental and numerical investigation of strain inhomogeneity in zirconia during a Brazilian test. *Int J Solids Struct* 256: 111978. https://doi.org/10.1016/j.ijsolstr.2022.111978.
35. Liu D, Zillhardt T, Earp P, et al. (2020) In situ measurement of elastic and total strains during ambient and high temperature deformation of a polygranular graphite. *Carbon* 163: 308-323. https://doi.org/10.1016/j.carbon.2020.03.020.
36. Lin L, Paul R, Hawkins C and Gallego NC (2023) Mechanical behavior analysis using small-size graphite disc compression testing with digital image correlation methods. *J Nucl Mater* 587: 154731. https://doi.org/10.1016/j.jnucmat.2023.154731.
37. Vervoort A, Min K-B, Konietzky H, et al. (2014) Failure of transversely isotropic rock under Brazilian test conditions. *Int J Rock Mech Min Sci* 70: 343-352. https://doi.org/10.1016/j.ijrmms.2014.04.006.
38. Liu C, Lovato ML, Stout MG and Huang Y (1997) Measurement of the fracture toughness of a fiber-reinforced composite using the Brazilian disk geometry. *Int J Fract* 87: 241-263. https://doi.org/10.1023/A:1007419406590.
39. Xu C, Han X, Cheng G, et al. (2018) Experimental study of ultra-high temperature interlaminar tensile strengths of 3D-needled C/C composites using the V-shaped notched specimen compression method. *Mech Mater* 126: 26-35. https://doi.org/10.1016/j.mechmat.2018.07.003.
40. Flores-Johnson EA, Irman K, Townsend J, et al. (2024) On the elastoplastic behaviour and fracture of graphite and C/C composites: Experiments and numerical simulations. In: ACAM2024 - 11th Australasian Congress on Applied Mechanics, Brisbane, Australia, 7-9 February 2024, pp. 81-87.
41. Yu J, Zhou C and Zhang H (2017) A micro-image based reconstructed finite element model of needle-punched C/C composite. *Compos Sci Technol* 153: 48-61. https://doi.org/10.1016/j.compscitech.2017.09.029.
42. Xie W, Yang F, Meng S, et al. (2020) Perforation of needle-punched carbon-carbon composites during high-temperature and high-velocity ballistic impacts. *Compos Struct* 245: 112224. https://doi.org/10.1016/j.compstruct.2020.112224.
43. Martin VA, Kraft RH, Hannah TH and Ellis S (2022) An energy-based study of the embedded element method for explicit dynamics. *Adv Model Simul Eng Sci* 9: 12. https://doi.org/10.1186/s40323-022-00223-x.
44. Häussler-Combe U, Shehni A and Chihadeh A (2020) Finite element modeling of fiber reinforced cement composites using strong discontinuity approach with explicit representation of fibers. *Int J Solids Struct* 200-201: 213-230. https://doi.org/10.1016/j.ijsolstr.2020.04.036.
45. Han M, Zhou C and Bi Q (2021) Residual mechanical properties of needle-punched carbon/carbon composites after oxidation. *Compos Commun* 28: 100966. https://doi.org/10.1016/j.coco.2021.100966.
46. TORAY. Technical Manual. https://www.toraycma.com/wp-content/uploads/Torayca-Technical-Manual_4-28-2020.pdf (accessed on 28 November 2024).
47. TENAX TEIJIN. Product Data Sheet. https://www.teijincarbon.com/fileadmin/user_upload/Datenbl%C3%A4tter/Filament_Yarn/Product_Data_Sheet_TSG01en__EU_Filament_.pdf (accessed on 28 November 2024).
48. Wang QZ, Jia XM, Kou SQ, et al. (2004) The flattened Brazilian disc specimen used for testing elastic modulus, tensile strength and fracture toughness of brittle rocks: analytical and numerical results. *Int J Rock Mech Min Sci* 41: 245-253. https://doi.org/10.1016/S1365-1609(03)00093-5.
49. Boyce S, Rougier E, Knight E, et al. (2021) Experimental study correlating damage and permeability in concrete using confined, flattened Brazilian disks. *Int J Damage Mech* 30: 1261-1280. https://doi.org/10.1177/1056789521998726.
50. SIMULIA (2022) SIMULIA User Assistance 2022. Abaqus 2022 Documentation. Dassault Systèmes. 2022.
51. Pinho S, Darvizeh R, Robinson P, et al. (2012) Material and structural response of polymer-matrix fibre-reinforced composites. *J Compos Mater* 46: 2313-2341. https://doi.org/10.1177/0021998312454478.

52. Jumahat A, Soutis C, Jones FR and Hodzic A (2010) Fracture mechanisms and failure analysis of carbon fibre/toughened epoxy composites subjected to compressive loading. *Compos Struct* 92: 295-305. https://doi.org/10.1016/j.compstruct.2009.08.010.
53. Toho (2010) TOHO TENAX HTS40 Carbon fibre, Technical Data Sheet. https://www.swiss-composite.ch/pdf/t-Tenax-Datenblatt.pdf, 2010 (accessed on 28 June 2023). 2010.
54. Chamis CC (1984) Mechanics of Composite Materials: Past, Present, and Future. In: 21st Annual Meeting of the Society for Engineering Science, Blacksburg, VA, USA, 15-17 October, 1984. https://ntrs.nasa.gov/citations/19880008360. 1984.
55. Wang Z, Wang B, Qin X, et al. (2022) The effect of fiber preform configuration on in-plane compressive behavior of high porosity needled carbon/carbon composites in elevated temperature environment. *Ceram Int* 48: 25355-25367. https://doi.org/10.1016/j.ceramint.2022.05.209.
56. Feih S and Mouritz AP (2012) Tensile properties of carbon fibres and carbon fibre–polymer composites in fire. *Compos Part A* 43: 765-772. https://doi.org/10.1016/j.compositesa.2011.06.016.
57. Davila CG, Camanho PP and Rose CA (2005) Failure Criteria for FRP Laminates. *J Compos Mater* 39: 323-345. https://doi.org/10.1177/0021998305046452.
58. Dávila CG and Camanho PP (2003) Failure Criteria for FRP Laminates in Plane Stress. Technical Report NASA/TM-2003-212663. NASA Langley Research Center, Virginia, USA. 2003.
59. Gouskos D and Iannucci L (2018) Finite Element Analysis of Non-Crimp Fabric Laminates under Compact Tension. In: ECCM18 - 18th European Conference on Composite Materials, Athens, Greece, 24-28 June 2018.
60. Pinho ST, Iannucci L and Robinson P (2006) Physically-based failure models and criteria for laminated fibre-reinforced composites with emphasis on fibre kinking: Part I: Development. *Compos Part A* 37: 63-73. https://doi.org/10.1016/j.compositesa.2005.04.016.
61. Gouskos D and Iannucci L (2022) A failure model for the analysis of cross-ply Non-Crimp Fabric (NCF) composites under in-plane loading: Experimental & numerical study. *Eng Fract Mech* 271: 108575. https://doi.org/10.1016/j.engfracmech.2022.108575.
62. Qi Y, Fang G, Wang Z, et al. (2020) An improved analytical method for calculating stiffness of 3D needled composites with different needle-punched processes. *Compos Struct* 237: 111938. https://doi.org/10.1016/j.compstruct.2020.111938.
63. Bradley LR, Bowen CR, McEnaney B and Johnson DC (2007) Shear properties of a carbon/carbon composite with non-woven felt and continuous fibre reinforcement layers. *Carbon* 45: 2178-2187. https://doi.org/10.1016/j.carbon.2007.06.072.
64. Halpin Affdl JC and Kardos JL (1976) The Halpin-Tsai equations: A review. *Polym Eng Sci* 16: 344-352. https://doi.org/10.1002/pen.760160512.
65. Halpin JC (1969) Stiffness and Expansion Estimates for Oriented Short Fiber Composites. *J Compos Mater* 3: 732-734. https://doi.org/10.1177/002199836900300419.
66. Tan Y, Yan Y, Li X and Guo F (2017) Numerical Analysis of the Elastic Properties of 3D Needled Carbon/Carbon Composites. *Mech Compos Mater* 53: 551-562. https://doi.org/10.1007/s11029-017-9685-5.
67. Tucker III CL and Liang E (1999) Stiffness predictions for unidirectional short-fiber composites: Review and evaluation. *Comp Sci Technol* 59: 655-671. https://doi.org/10.1016/S0266-3538(98)00120-1.
68. Lim HJ, Choi H, Lee MJ and Yun GJ (2021) An efficient multi-scale model for needle-punched Cf/SiCm composite materials with experimental validation. *Compos Part B* 217: 108890. https://doi.org/10.1016/j.compositesb.2021.108890.
69. Chen H, Na J, Wang D, et al. (2023) Numerical simulation and failure experiment of hygrothermal aged CFRP single and double lap joints. *Thin-Walled Struct* 188: 110786. https://doi.org/10.1016/j.tws.2023.110786.
70. Camanho PP and Dávila CG (2002) Mixed-Mode Decohesion Finite Elements for the Simulation of Delamination in Composite Materials. Technical Report NASA/TM-2002-211737. NASA Langley Research Center, Virginia, USA. 2002.
71. Tang Y, Ren Y, Zhao W, et al. (2022) Mechanical properties of all-C/C composite hybrid bonded/bolted joints. *J Reinf Plast Compos* 42: 377-390. https://doi.org/10.1177/07316844221127486.
72. Shi H-b, Tang M, Gao B and Su J-m (2011) Effect of graphitization parameters on the residual stress in 4D carbon fiber/carbon composites. *New Carbon Mater* 26: 287-292. https://doi.org/10.1016/S1872-5805(11)60082-6.
73. Rao MV, Mahajan P and Mittal RK (2008) Effect of architecture on mechanical properties of carbon/carbon composites. *Compos Struct* 83: 131-142. https://doi.org/10.1016/j.compstruct.2007.04.003.
74. Zhang F, Zhang H, Pan Z, et al. (2023) Analysis of tensile damage characteristics of single filled bolt hole in laminate. *Polym Compos* 44: 3153-3168. https://doi.org/10.1002/pc.27308.

75. Liu Y, Zhao H, Liu K, et al. (2024) Multi-scale modeling: Finite element analysis of the thermophysical properties of carbon/carbon composites considering manufacturing defects and porosity at high temperature. *J Compos Mater* 58: 3059-3075. 10.1177/00219983241289487.
76. Ge J, Qi L, Tian W, et al. (2023) Numerical evaluation of effective elastic properties of CVI-C/C composites considering anisotropic matrix. *Compos Struct* 306: 116561. https://doi.org/10.1016/j.compstruct.2022.116561.
77. Ge J, Chao X, Tian W, et al. (2024) Numerical mapping relationship between process parameters and mechanical properties of unidirectional carbon/carbon composites. *Int J Mech Sci* 267: 109008. https://doi.org/10.1016/j.ijmecsci.2024.109008.
78. Reiner J, Linden N, Vaziri R, et al. (2023) Bayesian parameter estimation for the inclusion of uncertainty in progressive damage simulation of composites. *Compos Struct* 321: 117257. https://doi.org/10.1016/j.compstruct.2023.117257.